

Non-linear version of stabilized conforming nodal integration for Galerkin mesh-free methods

Jiun-Shyan Chen^{*,†}, Sangpil Yoon[‡] and Cheng-Tang Wu[§]

*Department of Civil and Environmental Engineering, University of California, Los Angeles,
5713G Boelter Hall, Los Angeles, CA 90095, U.S.A.*

SUMMARY

A stabilized conforming (SC) nodal integration, which meets the integration constraint in the Galerkin mesh-free approximation, is generalized for non-linear problems. Using a Lagrangian discretization, the integration constraints for SC nodal integration are imposed in the undeformed configuration. This is accomplished by introducing a Lagrangian strain smoothing to the deformation gradient, and by performing a nodal integration in the undeformed configuration. The proposed method is independent to the path dependency of the materials. An assumed strain method is employed to formulate the discrete equilibrium equations, and the smoothed deformation gradient serves as the stabilization mechanism in the nodally integrated variational equation. Eigenvalue analysis demonstrated that the proposed strain smoothing provides a stabilization to the nodally integrated discrete equations. By employing Lagrangian shape functions, the computation of smoothed gradient matrix for deformation gradient is only necessary in the initial stage, and it can be stored and reused in the subsequent load steps. A significant gain in computational efficiency is achieved, as well as enhanced accuracy, in comparison with the mesh-free solution using Gauss integration. The performance of the proposed method is shown to be quite robust in dealing with non-uniform discretization. Copyright © 2002 John Wiley & Sons, Ltd.

KEY WORDS: nodal integration; stabilization method; mesh-free method; moving least square; reproducing kernel; non-linear mechanics

1. INTRODUCTION

The Galerkin approximation of weak forms using moving least-squares (MLS) [1, 2] or reproducing kernel (RK) [3] approximations are, in general, referred to as the Galerkin mesh-free methods [4–8], in that the approximation and discretization are constructed entirely using

*Correspondence to: Jiun-Shyan Chen, Department of Civil and Environmental Engineering, University of California, Los Angeles, 5713G Boelter Hall, Los Angeles, CA 90095, U.S.A.

†E-mail: jschen@seas.ucla.edu

‡E-mail: sangpil@seas.ucla.edu

§Livermore Software Technology Corporation, 7374 Las Positas Road, Livermore, CA 94550, U.S.A. E-mail: ctwu@lstc.com

Contract/grant sponsor: NSF; contract/grant number: CMS 97-13842

Contract/grant sponsor: NSF/DARPA OPAL; contract/grant number: DMS 98-74015

nodal information. This attribute is extremely attractive in engineering practice as it permits reduced restriction in the discretization of the problem domain. Nonetheless, domain integration methods compatible with MLS and RK mesh-free approximations have not been fully developed.

It has become apparent that shortcomings exist with respect to Gauss integration for Galerkin mesh-free methods for several reasons: (1) domain partitioning for integration must match the shape function supports to minimize integration errors [9], (2) the higher-order Gauss integration required for mesh-free computation is computationally inefficient, and (3) Gauss integration does not meet linear exactness in the Galerkin mesh-free approximation [10]. The requirements to achieve linear exactness in Galerkin approximation of Dirichlet boundary value problems are [10–12]:

$$\sum_I \nabla \Psi_I(\mathbf{x}) = \mathbf{0}, \quad \sum_I \nabla \Psi_I(\mathbf{x}) x_{iI} = \nabla x_i \quad (1)$$

$$\text{In}[\nabla \Psi_I(\mathbf{x})] = \mathbf{0} \quad \text{for all interior nodes} \quad (2)$$

where $\Psi_I(\mathbf{x})$ is the shape function for test and trial functions in the Galerkin approximation, and $\text{In}[\cdot]$ denotes numerical integration. Equation (1) can be met by employing linear basis functions in MLS or RK approximation, whereas Equation (2) represents the constraints on numerical integration. Although it can be easily shown that linear finite element shape functions meet the conditions in Equation (2), mesh-free methods using Gauss integration with shape functions constructed from MLS or RK approximation, in general, do not satisfy Equation (2). Another integration constraint, which occurs when natural boundary conditions exist, has also been presented in Reference [10] and will be discussed in Section 2. Similar discussions of the gradient operator in smoothed particle hydrodynamics (SPH) have been presented [13, 14].

Several nodal integration methods have been proposed to reduce computational effort in Galerkin mesh-free and collocation mesh-free methods. Beissel and Belytschko [15] considered adding a residual of the equilibrium equation to the potential energy functional as a stabilization of nodal integration. Numerical studies have been performed to investigate the appropriate selection of stabilization parameters. Bonet and Kulasegaram [12] introduced a least-squares stabilization in conjunction with an integration correction to satisfy Equation (2). The coefficients of integration corrections required to meet Equation (2) were determined using an iterative procedure. Chen *et al.* [10] proposed a stabilized conforming nodal integration in which a strain smoothing stabilization was introduced as a stabilization of nodal integration. This strain smoothing stabilization exactly satisfies Equation (2) for nodal integration, yielding a method that demonstrates superior accuracy to that of the Gauss integration in Galerkin mesh-free methods as shown in Reference [10].

Improvement of nodal integration in other non-Galerkin-type mesh-free methods has also been investigated. Randles *et al.* [16] proposed a stress point method under the framework of SPH. Stresses are computed away from nodal points for which the kernel functions have zero derivatives. Breitkopf *et al.* [17] proposed a double grid diffuse collocation method as an extension of the collocation approach originally introduced by Liszka and Orkisz [18] under a finite difference framework. In this method, the second-order derivatives in the strong form are computed from two first-order derivatives at two sets of discrete points.

The purpose of this paper is to develop a stabilized conforming nodal integration for general non-linear problems. In this approach, a Lagrangian description and discretization is employed in the Galerkin mesh-free method, and the variational equation is transformed to the undeformed configuration. To meet integration constraints and to provide a stabilization for a nodally integrated mesh-free discrete equation, an assumed deformation gradient, obtained using a Lagrangian strain smoothing of the displacement gradient, is introduced. The variational equation is formulated using the assumed strain method, in which potential energy is expressed in terms of displacement and the smoothed deformation gradient. The proposed method is applicable to both path-independent and path-dependent problems. The over-constrained conditions in the mesh-free approximation of incompressible problems can also be eliminated using the proposed nodal integration with strain smoothing stabilization.

In the following discussion, Section 2 reviews the mesh-free approximation methods, integration constraints, and stabilized conforming nodal integration for linear problems. An eigenvalue analysis is also performed to demonstrate how strain smoothing provides a stabilization to the nodally integrated mesh-free discrete equations. Section 3 introduces a strain smoothing stabilization to the deformation gradient and discusses the numerical procedures using a non-linear elastic model. The construction of the discrete equations using an assumed strain method and the proposed stabilized conforming nodal integration is presented. The extension of the stabilization method to plasticity is given in Section 4. Several examples are presented in Section 5, and conclusions are summarized in Section 6.

2. REVIEW OF STABILIZED CONFORMING NODAL INTEGRATION

2.1. MLS/RK approximation

The moving least-squares (MLS) [1, 2] and reproducing kernel (RK) [3] methods have been widely used as approximations of test and trial functions in the Galerkin mesh-free methods. These two approximation methods can be generalized in the following form:

$$u_i^h(\mathbf{x}) = \sum_{l=1}^{NP} C(\mathbf{x}; \mathbf{x} - \mathbf{x}_l) \Phi_a(\mathbf{x} - \mathbf{x}_l) d_{il} \quad (3)$$

where u_i^h is the approximation of the displacement u_i , d_{il} are the coefficients of approximation, NP is the number of discrete particles, $\Phi_a(\mathbf{x} - \mathbf{x}_l)$ is the kernel function that determines the smoothness and locality (compact support size 'a') of the approximation, and $C(\mathbf{x}; \mathbf{x} - \mathbf{x}_l)$ is the enrichment function used to facilitate completeness of the approximation [3]:

$$C(\mathbf{x}; \mathbf{x} - \mathbf{x}_l) = \sum_{i+j+k=0}^n b_{ijk}(\mathbf{x}) (x_1 - x_{1l})^i (x_2 - x_{2l})^j (x_3 - x_{3l})^k \quad (4)$$

where $\{(x_1 - x_{1l})^i (x_2 - x_{2l})^j (x_3 - x_{3l})^k\}_{i+j+k=0}^n$ are monomial basis functions. The coefficients $b_{ijk}(\mathbf{x})$ can be obtained by forcing Equation (3) to exactly reproduce the basis functions:

$$\sum_{l=1}^{NP} C(\mathbf{x}; \mathbf{x} - \mathbf{x}_l) \Phi_a(\mathbf{x} - \mathbf{x}_l) x_{1l}^i x_{2l}^j x_{3l}^k = x_1^i x_2^j x_3^k \quad \text{for } 0 \leq i + j + k \leq n \quad (5)$$

Or equivalently,

$$\sum_{I=1}^{\text{NP}} C(\mathbf{x}; \mathbf{x} - \mathbf{x}_I) \Phi_a(\mathbf{x} - \mathbf{x}_I) (x_1 - x_{1I})^i (x_2 - x_{2I})^j (x_3 - x_{3I})^k = \delta_{i0} \delta_{j0} \delta_{k0} \quad \text{for } 0 \leq i + j + k \leq n \quad (6)$$

Substituting the solution $b_{ijk}(\mathbf{x})$ obtained from Equation (6) into Equation (3) leads to

$$u_i^h(\mathbf{x}) = \sum_{I=1}^{\text{NP}} \Psi_I(\mathbf{x}) d_{iI} \quad (7)$$

$$\Psi_I(\mathbf{x}) = \mathbf{H}^T(\mathbf{0}) \mathbf{M}(\mathbf{x})^{-1} \mathbf{H}(\mathbf{x} - \mathbf{x}_I) \Phi_a(\mathbf{x} - \mathbf{x}_I) \quad (8)$$

$$\mathbf{H}^T(\mathbf{x} - \mathbf{x}_I) = [1, x_1 - x_{1I}, x_2 - x_{2I}, x_3 - x_{3I}, (x_1 - x_{1I})^2, \dots, (x_3 - x_{3I})^n] \quad (9a)$$

$$\mathbf{M}(\mathbf{x}) = \sum_{I=1}^{\text{NP}} \mathbf{H}(\mathbf{x} - \mathbf{x}_I) \mathbf{H}^T(\mathbf{x} - \mathbf{x}_I) \Phi_a(\mathbf{x} - \mathbf{x}_I) \quad (9b)$$

where $\Psi_I(\mathbf{x})$ are referred to as the shape functions of MLS/RK approximation. The smoothness of $\Psi_I(\mathbf{x})$ is the same as that of the kernel function $\Phi_a(\mathbf{x} - \mathbf{x}_I)$. A commonly used cubic B-spline kernel function is

$$\Phi_a(\mathbf{x} - \mathbf{x}_I) = \begin{cases} \frac{2}{3} - 4 \left(\frac{\|\mathbf{x} - \mathbf{x}_I\|}{a} \right)^2 + 4 \left(\frac{\|\mathbf{x} - \mathbf{x}_I\|}{a} \right)^3 & \text{for } 0 \leq \frac{\|\mathbf{x} - \mathbf{x}_I\|}{a} \leq \frac{1}{2} \\ \frac{4}{3} - 4 \left(\frac{\|\mathbf{x} - \mathbf{x}_I\|}{a} \right) + 4 \left(\frac{\|\mathbf{x} - \mathbf{x}_I\|}{a} \right)^2 - \frac{4}{3} \left(\frac{\|\mathbf{x} - \mathbf{x}_I\|}{a} \right)^3 & \text{for } \frac{1}{2} \leq \frac{\|\mathbf{x} - \mathbf{x}_I\|}{a} \leq 1 \\ 0 & \text{otherwise} \end{cases} \quad (10)$$

2.2. Integration constraints

Linear exactness in the Galerkin approximation requires (1) first-order completeness of the trial and test functions and (2) a spatial integration that satisfies integration constraints (IC). In an earlier paper, Chen *et al.* [10] imposed the requirement for a discrete displacement vector emanating from a linear displacement field $u_i^h = a_{i0} + a_{i1}x + a_{i2}y$ that the discrete equilibrium equation must be satisfied. This yields the integration constraints:

$$\sum_{L=1}^{\text{NIT}} \nabla \Psi_I(\hat{\mathbf{x}}_L) w_L = \mathbf{0} \quad \text{for } \{I: \text{supp}(\Psi_I) \cap \Gamma = \emptyset\} \quad (11)$$

$$\sum_{L=1}^{\text{NIT}} \nabla \Psi_I(\hat{\mathbf{x}}_L) w_L = \sum_{L=1}^{\text{NITh}} \mathbf{n} \Psi_I(\tilde{\mathbf{x}}_L) s_L \quad \text{for } \{I: \text{supp}(\Psi_I) \cap \Gamma^h \neq \emptyset\} \quad (12)$$

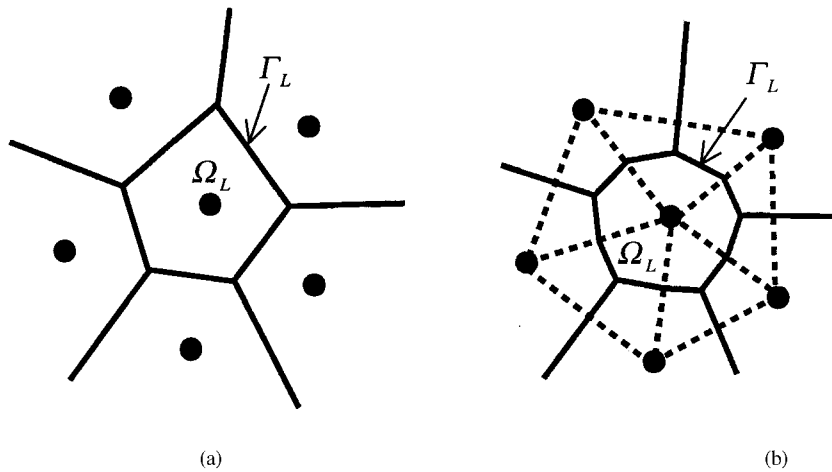


Figure 1. Nodal representative domain by: (a) Voronoi diagram; and (b) Delaunay triangulation.

where Γ^h is the natural boundary, Γ is the total boundary, \mathbf{n} is the surface normal on Γ^h , $\hat{\mathbf{x}}_L$ and w_L are the spatial co-ordinate and weight of the domain integration point, respectively, $\hat{\mathbf{x}}_L$ and s_L are the spatial co-ordinate and weight of natural boundary integration point, respectively, NIT is the number of integration points for domain integration and NIT_h is the number of integration points for natural boundary integration. This corresponds to a discrete condition PG2 in Krongauz and Belytschko [11]. No integration constraints are needed for shape functions that intersect with the essential boundaries. In the standard patch test, where all boundaries are essential boundaries, only Equation (11) is needed as a constraint for integration.

2.3. Strain smoothing stabilization

A strain smoothing [10] that meets integration constraints has been proposed to eliminate spurious oscillation that results from direct nodal integration of the weak form. It starts with a strain smoothing at the nodal representative domain by

$$\tilde{\nabla} u_i^h(\mathbf{x}_L) = \frac{1}{A_L} \int_{\Omega_L} \nabla u_i^h d\Omega, \quad A_L = \int_{\Omega_L} d\Omega \quad (13)$$

where Ω_L is a nodal representative domain and $\tilde{\nabla}$ is the smoothed gradient operator. Two methods have been used in the construction of the nodal representative domain. The first approach employs a Voronoi diagram, as shown in Figure 1(a). The second approach considers a Delaunay triangulation; the dual of a Voronoi diagram. In this second approach, the nodal representative domain is constructed by connecting the centroids of triangles and the middle points at the three edges of the triangle as shown in Figure 1(b). Other CAD triangulation tools can also be employed for the construction of the nodal representative domain.

It will be shown in subsequent discussion that satisfaction of the integration constraints can be made independent of the shape of the nodal representative domain. This is accomplished by applying divergence theorem to Equation (13) to yield

$$\tilde{\nabla} u_i^h(\mathbf{x}_L) = \frac{1}{A_L} \int_{\Gamma_L} \mathbf{n} u_i^h d\Gamma \quad (14)$$

where Γ_L is the boundary of the representative domain of node L as shown in Figure 1. Introducing RK shape functions into Equation (13) yields

$$\tilde{\nabla} u_i^h(\mathbf{x}_L) = \sum_I \tilde{\nabla} \Psi_I(\mathbf{x}_L) d_{iI} \quad (15)$$

where

$$\tilde{\nabla} \Psi_I(\mathbf{x}_L) = \frac{1}{A_L} \int_{\Omega_L} \nabla \Psi_I(\mathbf{x}) d\Omega = \frac{1}{A_L} \int_{\Gamma_L} \Psi_I(\mathbf{x}) \mathbf{n}(\mathbf{x}) d\Gamma \quad (16)$$

Here $\tilde{\nabla} \Psi_I(\mathbf{x}_L)$ is the smoothed $\nabla \Psi_I(\mathbf{x})$ evaluated at point \mathbf{x}_L . The boundary integration in Equation (16) can be performed by a simple trapezoidal rule as described in Reference [10]. It has been shown there that this smoothed shape function gradient $\tilde{\nabla} \Psi_I(\mathbf{x}_L)$ meets the integration constraint for nodal integration with weight A_L , i.e.,

$$\sum_{L=1}^{NIT} \tilde{\nabla} \Psi_I(\mathbf{x}_L) A_L = \mathbf{0} \quad \text{for } \{I: \text{supp}(\Psi_I) \cap \Gamma = \emptyset\} \quad (17)$$

and

$$\sum_{L=1}^{NIT} \tilde{\nabla} \Psi_I(\mathbf{x}_L) A_L = \sum_{K=1}^{NITh} \mathbf{n} \Psi_I(\mathbf{x}_K) s_K \quad \text{for } \{I: \text{supp}(\Psi_I) \cap \Gamma^h \neq \emptyset\} \quad (18)$$

Note that satisfying Equation (18) also requires the numerical integration on the natural boundary Γ^h to be identical to the boundary integration on Γ_L in Equation (16). *In this approach, the actual shape of the nodal representative domain has no influence in satisfying the integration constraints.*

The employment of smoothed shape function derivatives in Equation (16) as an approximation of strain provides a stabilization when the weak form is integrated nodally. This is demonstrated in an eigenvalue analysis of an elasticity stiffness matrix associated with a domain discretization shown in Figure 2. To study the nullity of the nodally integrated stiffness matrix, all nodes are free of constraints. When the stiffness matrix is constructed using a direct nodal integration without strain smoothing, there exist 4 eigenvectors associated with zero eigenvalue as shown in Figure 3 (zero energy modes). Mode shapes are plotted using a mesh for clarity. Among the 4 zero energy modes, 3 are rigid body modes, and the fourth one is an improper zero energy mode due to rank deficiency. With an employment of strain

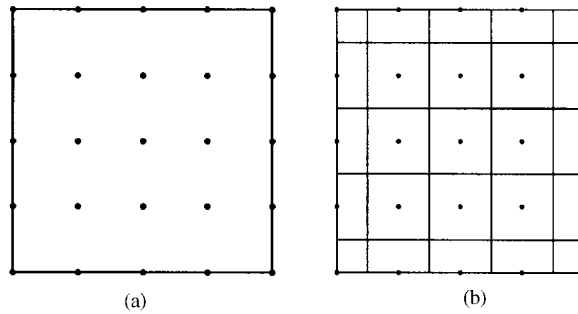


Figure 2. Discretization and nodal representative domain for nodal integration: (a) mesh-free discretization; and (b) nodal representative domain.

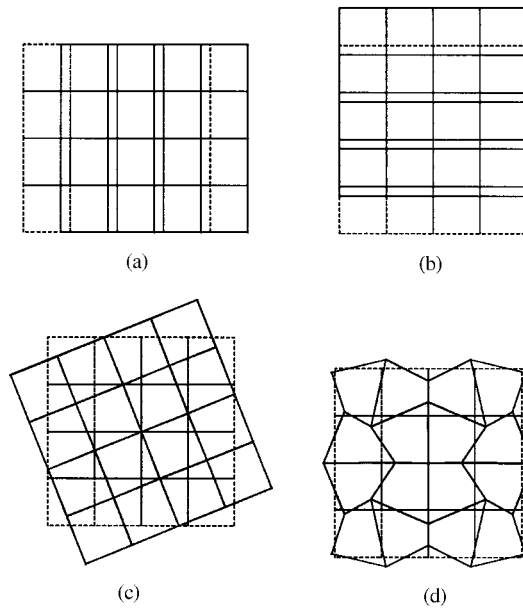


Figure 3. Four smallest eigenvalues (λ) and corresponding eigenvectors of a nodally integrated stiffness matrix without stabilization: (a) $\lambda = 0.0$: x -translation; (b) $\lambda = 0.0$: y -translation; (c) $\lambda = 0.0$: rotation; and (d) $\lambda = 0.0$: improper zero-energy mode.

smoothing, the nodally integrated stiffness matrix contains only 3 zero eigenvalues corresponding to rigid body modes, and the fourth smallest eigenvalue is non-zero and is associated with the deformation modes shown in Figure 4.

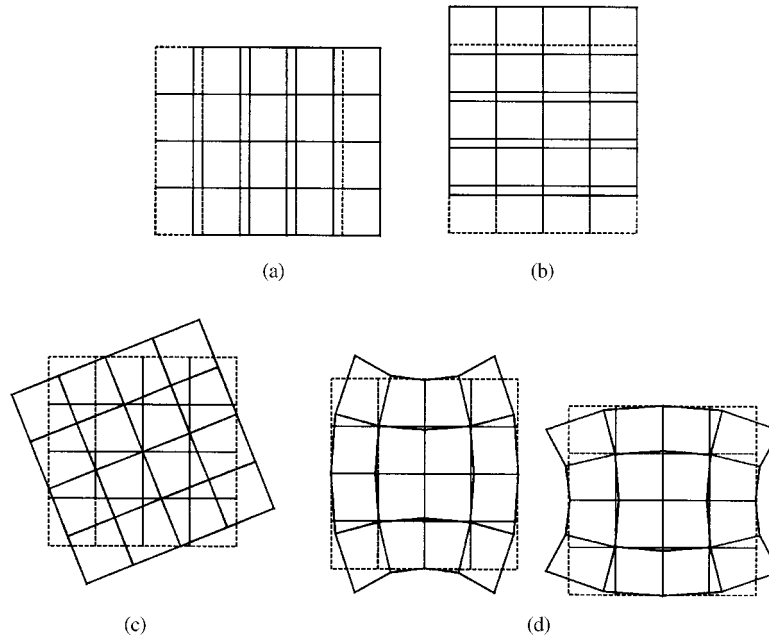


Figure 4. Four smallest eigenvalues (λ) and corresponding eigenvectors of a nodally integrated stiffness matrix with strain smoothing stabilization: (a) $\lambda = 0.0$: x -translation; (b) $\lambda = 0.0$: y -translation; (c) $\lambda = 0.0$: rotation; and (d) $\lambda = 0.1089$: two deformation modes.

3. STABILIZED CONFORMING NODAL INTEGRATION FOR NON-LINEAR ELASTICITY

3.1. Lagrangian–Galerkin mesh-free discretization

A Lagrangian–Galerkin mesh-free approximation and discretization [19] is employed herein to develop a stabilized conforming nodal integration for non-linear problems. In the Lagrangian approach, the MLS/RK approximation of displacement u_i is defined using the material co-ordinate \mathbf{X} as

$$u_i^h(\mathbf{X}, t) = \sum_{I=1}^{\text{NP}} C(\mathbf{X}; \mathbf{X} - \mathbf{X}_I) \Phi_a(\mathbf{X} - \mathbf{X}_I) d_{il}(t) \quad (19)$$

$$C(\mathbf{X}; \mathbf{X} - \mathbf{X}_I) = \sum_{i+j+k=0}^n b_{ijk}(\mathbf{X}) (X_1 - X_{1I})^i (X_2 - X_{2I})^j (X_3 - X_{3I})^k \quad (20)$$

Imposition of the exact reproduction of the monomial basis in material co-ordinates yields the following Lagrangian shape function:

$$u_i^h(\mathbf{X}, t) = \sum_{I=1}^{\text{NP}} \Psi_I(\mathbf{X}) d_{il}(t) \quad (21)$$

$$\Psi_I(\mathbf{X}) = \mathbf{H}^T(\mathbf{0})\mathbf{M}^{-1}(\mathbf{X})\mathbf{H}(\mathbf{X} - \mathbf{X}_I)\Phi_a(\mathbf{X} - \mathbf{X}_I) \quad (22)$$

$$\mathbf{M}(\mathbf{X}) = \sum_{I=1}^{\text{NP}} \mathbf{H}(\mathbf{X} - \mathbf{X}_I)\mathbf{H}^T(\mathbf{X} - \mathbf{X}_I)\Phi_a(\mathbf{X} - \mathbf{X}_I) \quad (23)$$

$$\mathbf{H}^T(\mathbf{X} - \mathbf{X}_I) = [1, X_1 - X_{1I}, X_2 - X_{2I}, X_3 - X_{3I}, \dots, (X_3 - X_{3I})^n] \quad (24)$$

Note that this set of Lagrangian MLS/RK shape functions satisfies the consistency conditions in the material co-ordinate:

$$\sum_{I=1}^{\text{NP}} \Psi_I(\mathbf{X})X_{1I}^i X_{2I}^j X_{3I}^k = X_1^i X_2^j X_3^k, \quad 0 \leq i + j + k \leq n \quad (25)$$

The variational equation for a general non-linear boundary value problem can be expressed as

$$\int_{\Omega_X} \delta F_{ij} \sigma_{ij} \, d\Omega - \delta W^{\text{ext}} = 0 \quad (26)$$

where $F_{ij} = \partial u_i / \partial X_j + \delta_{ij}$ is the deformation gradient, σ_{ij} is the first Piola–Kirchhoff stress, Ω_X is the domain of the undeformed configuration and W^{ext} is the external work. For non-linear problems, achievement of an exact solution in the Galerkin approximation of a boundary value problem with solution $u_i = a_{i0} + a_{i1}X_1 + a_{i2}X_2$, requires (1) the shape functions $\Psi_I(\mathbf{X})$ in Equation (21) hold linear consistency in the material co-ordinate and (2) the gradient matrix associated with the deformation gradient \mathbf{F} meets the integration constraints in Equations (11) and (12) in the undeformed configuration. Note that Equation (26) is applicable to both path-independent and path-dependent materials; the same integration constraints can be applied to both cases.

3.2. Lagrangian strain smoothing of deformation gradient

Non-linear elastic material is a typical path-independent material, where the internal energy of the material can be expressed in terms of the deformation gradient. To meet integration constraints for nodal integration of Equation (26) using the deformation gradient as the primary kinematic variable, the Lagrangian strain smoothing of deformation gradient at a nodal point with material co-ordinate \mathbf{X}_L is considered:

$$\tilde{F}_{ij}(\mathbf{X}_L) = \frac{1}{A_L^X} \int_{\Omega_L^X} \left(\frac{\partial u_i^h}{\partial X_j} + \delta_{ij} \right) \, d\Omega = \frac{1}{A_L^X} \int_{\Omega_L^X} \left(\frac{\partial u_i^h}{\partial X_j} \right) \, d\Omega + \delta_{ij} \quad (27)$$

$$A_L^X = \int_{\Omega_L^X} \, d\Omega \quad (28)$$

where Ω_L^X is the nodal representative domain of \mathbf{X}_L in the undeformed configuration. Applying the divergence theorem at the undeformed configuration yields

$$\tilde{F}_{ij}(\mathbf{X}_L) = \frac{1}{A_L^X} \int_{\Gamma_L^X} (u_i^h N_j) \, d\Gamma + \delta_{ij} \equiv \tilde{e}_{ij}(\mathbf{X}_L) + \delta_{ij} \quad (29)$$

where

$$\tilde{e}_{ij}(\mathbf{X}_L) = \frac{1}{A_L^X} \int_{\Gamma_L^X} (u_i^h N_j) d\Gamma \quad (30)$$

In Equation (30), Γ_L^X is the boundary of Ω_L^X and \mathbf{N} is the surface normal of Γ_L^X in the undeformed configuration. Introducing a Lagrangian shape function into Equation (30) yields

$$\tilde{e}_{ij}(\mathbf{X}_L) = \sum_I \tilde{b}_{ji}^L d_{iI} \quad (31)$$

where

$$\tilde{b}_{ji}^L = \frac{1}{A_L^X} \int_{\Gamma_L^X} (\Psi_I N_j) d\Gamma \quad (32)$$

Using a similar analogy as in Reference [10], it can be easily shown that the gradient matrix associated with this smoothed deformation gradient meets the integration constraints of nodal integration for Equation (26) in the undeformed configuration.

Using strain smoothing in \tilde{F}_{ij} , $\Delta \tilde{F}_{ij}$ and $\delta \tilde{F}_{ij}$ at \mathbf{X}_L are obtained by

$$\Delta \tilde{F}_{ij}(\mathbf{X}_L) = \Delta \tilde{e}_{ij}(\mathbf{X}_L) = \sum_I \tilde{b}_{ji}^L \Delta d_{iI} \quad (33)$$

$$\delta \tilde{F}_{ij}(\mathbf{X}_L) = \delta \tilde{e}_{ij}(\mathbf{X}_L) = \sum_I \tilde{b}_{ji}^L \delta d_{iI} \quad (34)$$

Similar to linear problems [10], the strain smoothing meets integration constraints in nodal integration regardless of the type of numerical boundary integration for the smoothed strain in Equation (32). Therefore, the boundary integration of \tilde{b}_{ji}^L in Equation (32) can be accomplished using a simple Trapezoidal rule on each segment of $\Gamma_L^X = \Gamma_{L_1}^X \cup \Gamma_{L_2}^X \cdots \cup \Gamma_{L_m}^X$:

$$\int_{\Gamma_L^X} (\Psi_I N_j) d\Gamma = \int_{\Gamma_{L_1}^X \cup \Gamma_{L_2}^X \cdots \cup \Gamma_{L_m}^X} (\Psi_I N_j) d\Gamma = \sum_{n=1}^m \int_{\Gamma_{L_n}^X} (\Psi_I N_j) d\Gamma \quad (35)$$

and

$$\int_{\Gamma_{L_n}^X} (\Psi_I N_j) d\Gamma = \sum_{\ell=1}^{\text{NINTn}} \Psi_I(\mathbf{X}_\ell^n) N_j^n s_\ell^n \quad (36)$$

where \mathbf{N}^n is the surface outward normal of segment $\Gamma_{L_n}^X$, \mathbf{X}_ℓ^n and s_ℓ^n are the integration point and weight on $\Gamma_{L_n}^X$, respectively and NINTn is the number of integration points on $\Gamma_{L_n}^X$.

3.3. Galerkin approximation and discretization for non-linear elastic materials

The formulation for a non-linear elastic material is first considered. To introduce the smoothed deformation gradient into the Galerkin approximation, an assumed strain method is employed, in which the potential energy of a non-linear elasticity problem is expressed as

$$\Pi(\mathbf{u}, \tilde{\mathbf{F}}) = \int_{\Omega_X} W(\tilde{\mathbf{F}}) d\Omega - W^{\text{ext}}(\mathbf{u}) \quad (37)$$

where W is the strain energy density function and W^{ext} is the external work due to surface traction and body force. Minimization of potential energy leads to the following variational equation:

$$\delta\Pi(\mathbf{u}, \tilde{\mathbf{F}}) = \int_{\Omega_X} \delta\tilde{F}_{ij} \frac{\partial W(\tilde{\mathbf{F}})}{\partial \tilde{F}_{ij}} d\Omega - \delta W^{\text{ext}}(\mathbf{u}) = \int_{\Omega_X} \delta\tilde{e}_{ij} \tilde{\sigma}_{ij}(\tilde{\mathbf{F}}) d\Omega - \delta W^{\text{ext}}(\mathbf{u}) = 0 \quad (38)$$

where $\tilde{\sigma}_{ij}(\tilde{\mathbf{F}}) = \partial W(\tilde{\mathbf{F}}) / \partial \tilde{F}_{ij}$ is the smoothed first Piola–Kirchhoff stress. The linearization of Equation (38) yields

$$\begin{aligned} \Delta\delta\Pi(\mathbf{u}, \tilde{\mathbf{F}}) &= \int_{\Omega_X} \delta\tilde{e}_{ij} \frac{\partial^2 W(\tilde{\mathbf{F}})}{\partial \tilde{F}_{ij} \partial \tilde{F}_{kl}} \Delta\tilde{e}_{kl} d\Omega - \Delta\delta W^{\text{ext}}(\mathbf{u}) \\ &= \int_{\Omega_X} \delta\tilde{e}_{ij} [\tilde{C}_{ijkl}^{\sigma}(\tilde{\mathbf{F}}) + \tilde{T}_{ijkl}^{\sigma}(\tilde{\mathbf{F}})] \Delta\tilde{e}_{kl} d\Omega - \Delta\delta W^{\text{ext}}(\mathbf{u}) \end{aligned} \quad (39)$$

where

$$\tilde{C}_{ijkl}^{\sigma}(\tilde{\mathbf{F}}) = \tilde{F}_{im} \tilde{F}_{kn} \frac{\partial^2 W(\tilde{\mathbf{F}})}{\partial \tilde{E}_{mj} \partial \tilde{E}_{nl}}, \quad \tilde{E}_{ij} = \frac{1}{2} (\tilde{F}_{ki} \tilde{F}_{kj} - \delta_{ij}) \quad (40)$$

$$\tilde{T}_{ijkl}^{\sigma}(\tilde{\mathbf{F}}) = \delta_{ik} \tilde{F}_{mj} \tilde{\sigma}_{ml}(\tilde{\mathbf{F}}), \quad \tilde{\sigma}_{ij} = \frac{\partial W(\tilde{\mathbf{F}})}{\partial \tilde{F}_{ij}} \quad (41)$$

Introducing an approximation of the smoothed deformation gradient in Equation (31), and employing a nodal integration in Equations (38) and (39), the resulting incremental matrix equation is

$$\mathbf{K} \Delta \mathbf{d} = \mathbf{f}^{\text{ext}} - \mathbf{f}^{\text{int}} \quad (42)$$

where the external force vector \mathbf{f}^{ext} is constructed using the MLS/RK Lagrangian shape functions, and the stiffness matrix \mathbf{K} and internal force vector \mathbf{f}^{int} are nodally integrated using the smoothed deformation gradient in Equations (38) and (39) as

$$\mathbf{K}_{IJ} = \sum_{L=1}^{\text{NP}} \tilde{\mathbf{B}}_I^T(\mathbf{X}_L) [\tilde{\mathbf{C}}^{\sigma}(\tilde{\mathbf{F}}(\mathbf{X}_L)) + \tilde{\mathbf{T}}^{\sigma}(\tilde{\mathbf{F}}(\mathbf{X}_L))] \tilde{\mathbf{B}}_J(\mathbf{X}_L) A_L \quad (43)$$

$$\mathbf{f}_I^{\text{int}} = \sum_{L=1}^{\text{NP}} \tilde{\mathbf{B}}_I^T(\mathbf{X}_L) \tilde{\boldsymbol{\sigma}}(\tilde{\mathbf{F}}(\mathbf{X}_L)) A_L \quad (44)$$

where

$$\tilde{\mathbf{B}}_I(\mathbf{X}_L) = \begin{bmatrix} \tilde{b}_{1I}^L & 0 \\ 0 & \tilde{b}_{2I}^L \\ \tilde{b}_{2I}^L & 0 \\ 0 & \tilde{b}_{1I}^L \end{bmatrix} \quad (45)$$

$$\tilde{\boldsymbol{\sigma}} = \begin{bmatrix} \tilde{\sigma}_{11} \\ \tilde{\sigma}_{22} \\ \tilde{\sigma}_{12} \\ \tilde{\sigma}_{21} \end{bmatrix} \quad (46)$$

Note that the value of $\tilde{\mathbf{B}}_I$ evaluated at the material integration point \mathbf{X}_L does not change with the material deformation and can therefore be stored and reused for computing $\tilde{\mathbf{F}}(\mathbf{X}_L)$, \mathbf{K} and \mathbf{f}^{int} in each load step.

For an axisymmetric problem, the circumferential component $F_{33} \equiv F_{\theta\theta} = u_r/R + 1$ must be considered, therefore, an additional row $[\Psi_I/R, 0]$ is added to $\tilde{\mathbf{B}}_I$ (denoting $r \equiv x_1$, $R \equiv X_1$). The stabilization for $F_{\theta\theta}$ is not considered, hence Ψ_I/R is evaluated nodally in the construction of \mathbf{K} and \mathbf{f}^{int} . In the limiting case where the nodal point \mathbf{X}_L is located at the axis of axisymmetry (i.e. $X_{1L} = R_L \rightarrow 0$), the nodal value of u_r/R is computed by $\lim_{R \rightarrow 0} (u_r/R) = \partial u_r / \partial R$, since $u_r \rightarrow 0$ as $R \rightarrow 0$. Consequently, $[(\Psi_I/R)|_{\mathbf{X}_L}, 0]$ in $\tilde{\mathbf{B}}_I$ is calculated by $[\partial \Psi_I / \partial R|_{\mathbf{X}_L}, 0]$ for this case.

4. EXTENSION TO PLASTICITY

4.1. Lagrangian mesh-free approximation of path-dependent problems

Consider here the variational equation of an updated Lagrangian formulation with reference to the current configuration:

$$\delta \Pi = \int_{\Omega_x} \delta u_{i,j} \tau_{ij} \, d\Omega - \delta W^{\text{ext}} \quad (47)$$

where τ_{ij} is the Cauchy stress, $u_{i,j} \equiv \partial u_i / \partial x_j$, \mathbf{x} is the spatial co-ordinate related to the material co-ordinate \mathbf{X} by $x_i = X_i + u_i$ and Ω_x is the domain of the current configuration. Note that in Equation (47), the Cauchy stress τ_{ij} is a stress measure defined at the current configuration. The linearization of Equation (47) is

$$\Delta \delta \Pi = \int_{\Omega_x} \delta u_{i,j} (C_{ijkl}^\tau + T_{ijkl}^\tau) \Delta u_{k,l} \, d\Omega - \Delta \delta W^{\text{ext}} \quad (48)$$

where T_{ijkl}^τ is geometric response tensor given by

$$T_{ijkl}^\tau = \delta_{ik} \tau_{jl} \quad (49)$$

and C_{ijkl}^τ is the material response tensor that is closely related to the employment of the objective stress rates and their relationships with the Cauchy stress τ . To employ the Lagrangian shape function $\Psi_I(\mathbf{X})$, the variational equations (47) and (48) are transformed to the undeformed configuration Ω_X as

$$\int_{\Omega_X} \delta u_{i,j} \tau_{ij} d\Omega = \int_{\Omega_X} \frac{\partial \delta u_i}{\partial X_k} F_{kj}^{-1} \tau_{ij} J^0 d\Omega \quad (50)$$

and

$$\int_{\Omega_X} \delta u_{i,j} (C_{ijkl}^\tau + T_{ijkl}^\tau) \Delta u_{k,l} d\Omega = \int_{\Omega_X} \frac{\partial \delta u_i}{\partial X_m} F_{mj}^{-1} (C_{ijkl}^\tau + T_{ijkl}^\tau) F_{nl}^{-1} \frac{\partial \Delta u_k}{\partial X_n} J^0 d\Omega \quad (51)$$

where $J^0 = \det(\mathbf{F})$. In Equations (50) and (51), the strain measure $\partial u_i / \partial x_j$ in Equations (47) and (48) is replaced by $\partial u_i / \partial X_j$ which is subjected to a spatial derivative with respect to the material co-ordinate, $F_{kj}^{-1} \tau_{ij} J^0$ is the first Piola–Kirchhoff stress, and the domain is transformed to the undeformed configuration Ω_X . Although \mathbf{F}^{-1} requires taking derivatives with respect to the spatial co-ordinate \mathbf{x} in Equations (50) and (51), computationally, \mathbf{F}^{-1} is calculated at the integration point obtained by taking the inverse of \mathbf{F} pointwise.

4.2. Lagrangian strain smoothing for path-dependent problems

To introduce the Lagrangian shape function into the approximation of a path-dependent problem, the strain increment $\Delta u_{i,j}$ is computed by

$$\Delta u_{i,j} = \frac{\partial \Delta u_i}{\partial x_j} = \frac{\partial \Delta u_i}{\partial X_k} F_{kj}^{-1} = \Delta F_{ik} F_{kj}^{-1} \quad (52)$$

The strain smoothing of $\Delta u_{i,j}$ at the nodal sampling point \mathbf{X}_L in Equation (52) is computed by

$$\Delta \tilde{u}_{i,j}(\mathbf{X}_L) = \Delta \tilde{F}_{ij}(\mathbf{X}_L) \tilde{F}_{kj}^{-1}(\mathbf{X}_L) \quad (53)$$

where $\tilde{\mathbf{F}}^{-1}(\mathbf{X}_L)$ is the inverse of the smoothed deformation gradient $\tilde{\mathbf{F}}(\mathbf{X}_L)$ computed by following Equations (27)–(30) and $\Delta \tilde{\mathbf{F}}(\mathbf{X}_K)$ is expressed in terms of the smoothed gradient matrix according to Equation (33). Introducing a Lagrangian shape function to \mathbf{u} in Equation (52) yields

$$\Delta \tilde{u}_{i,j}(\mathbf{X}_L) = \left[\sum_I \tilde{b}_{kl}^L \Delta d_{il} \right] \tilde{F}_{kj}^{-1}(\mathbf{X}_L) \quad (54)$$

where in \tilde{b}_{kl}^L , \mathbf{N} is the surface normal of the nodal representative boundary Γ_L^X of node \mathbf{X}_L defined in the undeformed configuration.

4.3. Galerkin approximation and discretization

To introduce strain smoothing as an approximation of strain, an assumed strain method is employed to formulate the variational equation and its linearization:

$$\delta \Pi(\mathbf{u}, \tilde{\mathbf{F}}) = \int_{\Omega_X} \delta \tilde{F}_{ik} \tilde{F}_{kj}^{-1} \tilde{\tau}_{ij}(\tilde{\mathbf{F}}) \tilde{J}^0(\tilde{\mathbf{F}}) d\Omega - \delta W^{\text{ext}}(\mathbf{u}) \quad (55)$$

and

$$\Delta\delta\Pi(\mathbf{u}, \tilde{\mathbf{F}}) = \int_{\Omega_X} \delta\tilde{F}_{im}\tilde{F}_{mj}^{-1}[\tilde{C}_{ijkl}^\tau(\tilde{\mathbf{F}}) + \tilde{T}_{ijkl}^\tau(\tilde{\mathbf{F}})]\tilde{F}_{nl}^{-1}\Delta\tilde{F}_{kn}\tilde{J}^0(\tilde{\mathbf{F}})d\Omega - \Delta\delta W^{\text{ext}}(\mathbf{u}) \quad (56)$$

Introducing an approximation of the smoothed deformation gradient in Equations (29), (33) and (34), and employing nodal integration in Equations (55) and (56), the stiffness matrix \mathbf{K} and internal force vector \mathbf{f}^{int} are obtained by

$$\mathbf{K}_{IJ} = \sum_{L=1}^{\text{NP}} \tilde{\mathbf{B}}_I^T(\mathbf{X}_L)\tilde{\mathbf{G}}^T(\mathbf{X}_L)[\tilde{\mathbf{C}}^\tau(\tilde{\mathbf{F}}(\mathbf{X}_L)) + \tilde{\mathbf{T}}^\tau(\tilde{\mathbf{F}}(\mathbf{X}_L))]\tilde{\mathbf{G}}(\mathbf{X}_L)\tilde{\mathbf{B}}_J(\mathbf{X}_L)\tilde{J}^0(\mathbf{X}_L)A_L \quad (57)$$

$$\mathbf{f}_I^{\text{int}} = \sum_{L=1}^{\text{NP}} \tilde{\mathbf{B}}_I^T(\mathbf{X}_L)\tilde{\mathbf{G}}^T(\mathbf{X}_L)\tilde{\boldsymbol{\tau}}(\tilde{\mathbf{F}}(\mathbf{X}_L))\tilde{J}^0(\mathbf{X}_L)A_L \quad (58)$$

where

$$\tilde{\mathbf{G}} = \begin{bmatrix} \tilde{F}_{11}^{-1} & 0 & \tilde{F}_{21}^{-1} & 0 \\ 0 & \tilde{F}_{22}^{-1} & 0 & \tilde{F}_{12}^{-1} \\ \tilde{F}_{12}^{-1} & \tilde{F}_{21}^{-1} & \tilde{F}_{22}^{-1} & \tilde{F}_{11}^{-1} \end{bmatrix} \quad (59)$$

$$\tilde{\boldsymbol{\tau}} = \begin{bmatrix} \tilde{\tau}_{11} \\ \tilde{\tau}_{22} \\ \tilde{\tau}_{12} \end{bmatrix} \quad (60)$$

and $\tilde{\mathbf{B}}_I$ is the gradient matrix associated with the smoothed deformation gradient given in Equation (30). Using the Lagrangian approach, the value of $\tilde{\mathbf{B}}_I$ evaluated at the material integration point \mathbf{X}_L again does not change with the material deformation, and can therefore be stored and reused for computing $\tilde{\mathbf{F}}(\mathbf{X}_L)$, $\tilde{\mathbf{F}}^{-1}(\mathbf{X}_L)$, \mathbf{K} , and \mathbf{f}^{int} in each load step.

5. NUMERICAL EXAMPLES

MLS/RK approximation with linear basis functions is employed to formulate the mesh-free discrete equation in the following examples. Domain integration in the Galerkin approximation is performed using both the stabilized conforming (SC) nodal integration and the 5×5 Gauss integration methods for comparison. In Gauss integration, every four nodes form an integration cell in uniform discretizations, whereas three-node cell is used for non-uniform discretization. In the following, normalized support size R referred to support size normalized with averaged nodal distance.

5.1. Shallow arch under a concentrated load

The problem statement, boundary conditions, and geometry of a shallow arch subjected to a concentrated load are shown in Figure 5. A Saint Venant–Kirchhoff elastic material with

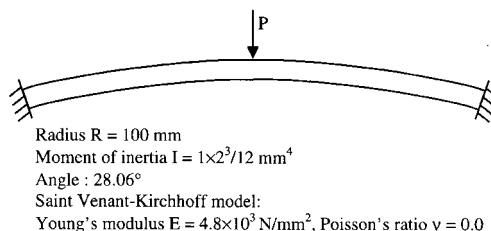


Figure 5. Problem statement of shallow arch under concentrated load.

geometric non-linearity is considered in which the strain energy density function is given by

$$W = \frac{1}{2} E_{ij} C_{ijkl} E_{kl}, \quad C_{ijkl} = \lambda \delta_{ij} \delta_{kl} + \mu (\delta_{ik} \delta_{jl} + \delta_{il} \delta_{jk}) \quad (61)$$

where λ and μ are Lamé's constants and \mathbf{E} is the Green–Lagrangian strain.

In this example, three uniformly refined discretizations (11×5 , 21×9 , 31×13 nodes) of a half-model are used to examine the convergence of the SC nodal integration method. A 5×5 quadrature is used in the Gauss integration for comparison, where four-node finite element mesh is employed as the integration cell. The SC nodal integration and Gauss integration solutions are compared with the analytical solution [20] using three model refinements and two normalized support sizes $R=1.0$ and 2.0 in Figures 6(a)–6(c). In all three discretizations, the SC nodal integration method generates a more accurate solution than the Gauss integration method, particularly for the coarse model with small R , where there is significant difference in the accuracy of the two integration methods. As the model is refined, the difference between the SC nodal integration and Gauss integration methods decreases. It is also observed that the SC nodal integration provides a more stable solution with respect to the change in shape function support size than the Gauss integration. Figure 7 shows that the use of a reduced quadrature order in the Gauss integration yields only a marginal improvement in accuracy.

The performance of the SC nodal integration method is also demonstrated for a non-uniform model of 105 nodes as shown in Figure 8. Constant support sizes of $a=2.0$ and 0.5 in the horizontal and vertical directions, respectively, are used according to the maximum nodal distance in the model. The representative nodal domain for SC nodal integration is obtained from a Voronoi diagram and a Delaunay triangulation method as shown in Figure 8. Figure 9 shows that SC nodal integration again provides a better solution than Gauss integration. It can also be seen that the arrangement of the nodal representative domain has little influence on the SC nodal integration solution. The Delaunay triangulation is also used to construct a finite element mesh for triangular elements displayed in Figure 8. Results show a severe locking in the finite element solution as shown in Figure 9. A comparison of normalized CPU times (normalized with respect to 2×2 Gauss integration of the 55-node model), excluding solution of linear equations, is presented in Figure 10.

5.2. Large deflection of a cantilever beam subjected to a tip shear load

In this example, the large deflection of a cantilever beam shown in Figure 11 is analysed. The beam is made of an elastic material, as described by Equation (61), and subjected to large

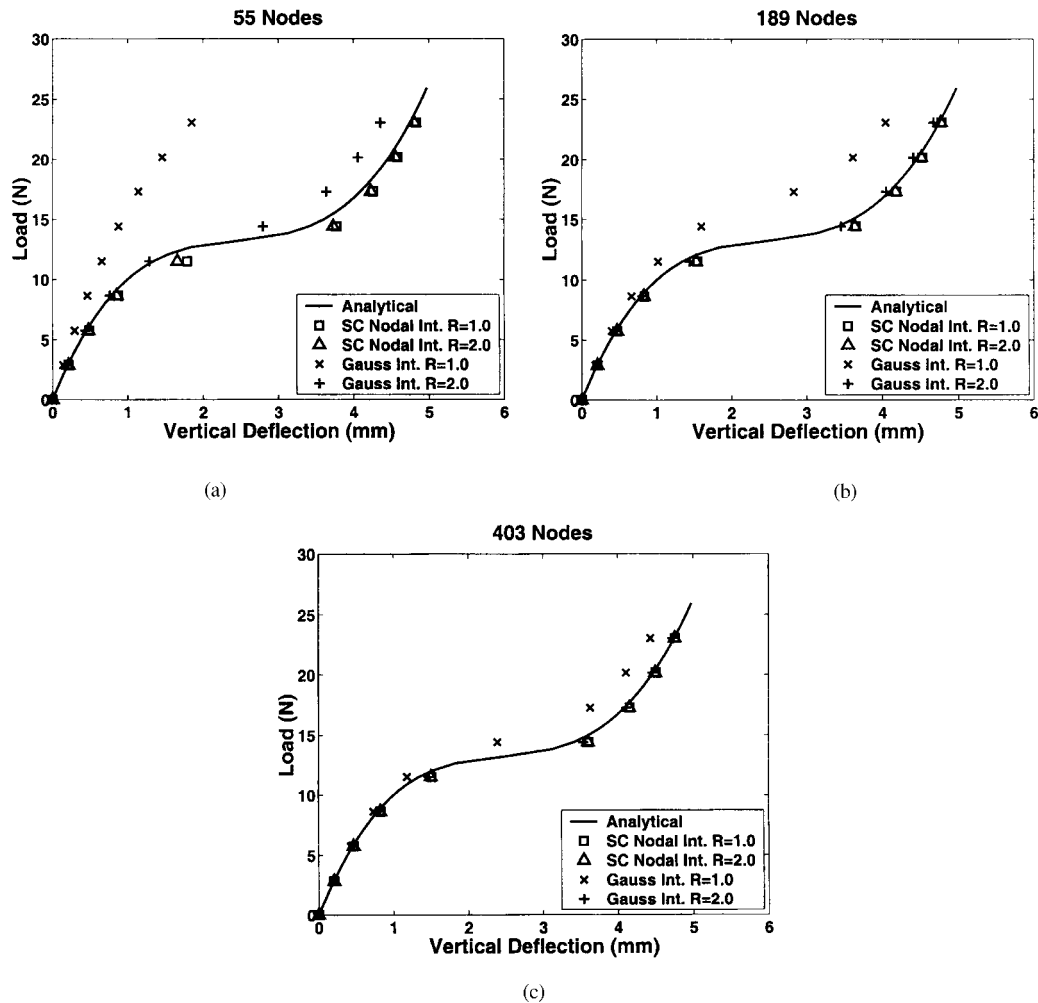


Figure 6. Comparison of SC nodal and Gauss integration methods in arch problem using three discretizations: (a) 11×5 nodes; (b) 21×9 nodes; and (c) 31×13 nodes.

deflection. Three levels of model refinements are used, with 21×3 , 41×5 and 61×7 equally spaced nodes. Normalized support sizes of $R = 1.0$ and 2.0 are used for each discretization. The analysis is carried out using 10 equal loading steps. The analytical solution of this problem can be found in Timoshenko *et al.* [21].

Both the SC nodal integration and a Gauss integration with a 5×5 quadrature are compared with the analytical solution in the analysis. Figures 12(a)–12(c) compare load–deflection curves for different discretizations and normalized shape function support sizes R . The SC nodal integration method exhibits better performance, especially for a coarse model. The robustness of the SC nodal integration method is more evident when a small shape function support size is used. A non-uniform 205-node model, as shown in Figure 13, has been

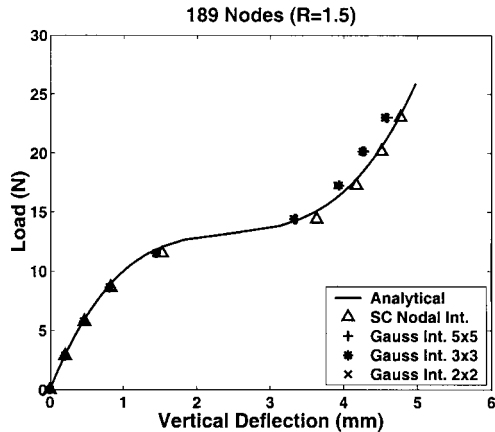


Figure 7. Effect of integration order in Gauss integration method.

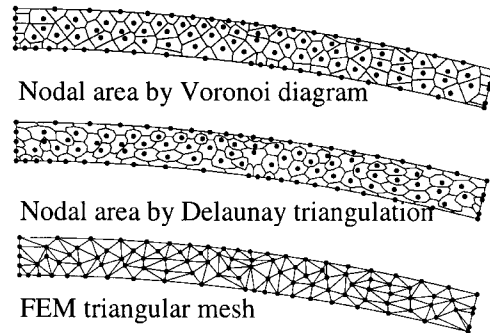


Figure 8. Irregular models for mesh-free and finite element analysis.

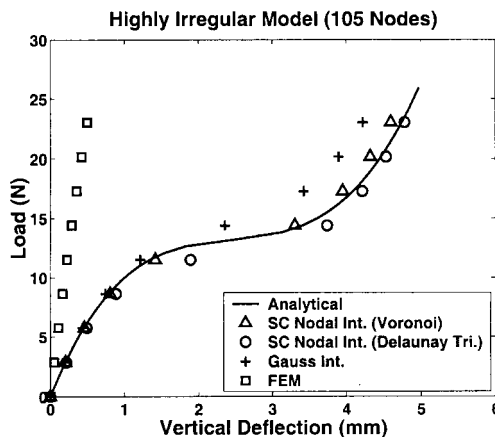


Figure 9. Solution of irregular discretization.

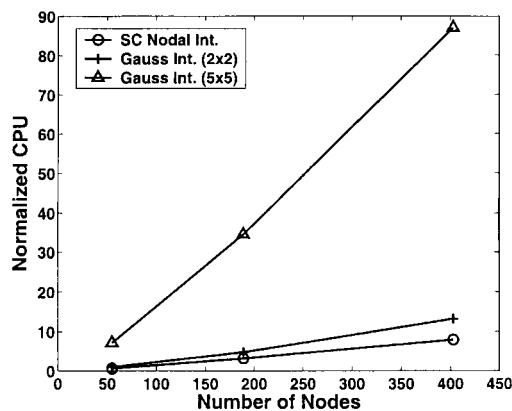


Figure 10. CPU comparison on integration methods in forming mesh-free discrete equations.

created to demonstrate the performance of SC nodal integration method under non-uniform discretization. In this example, representative nodal domains, generated by both Voronoi diagram and Delaunay triangulation, are employed in SC nodal integration. The load–deflection curves shown in Figure 13 demonstrate that a more accurate solution can be obtained using SC nodal integration. The results also show that the shapes of the representative nodal domains have only a marginal influence on the SC nodal integration solution. A comparison of normalized CPU times (normalized with respect to Gauss integration of the 63-node model), excluding solution of linear equations, is presented in Figure 14.

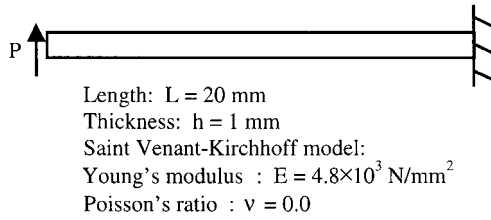
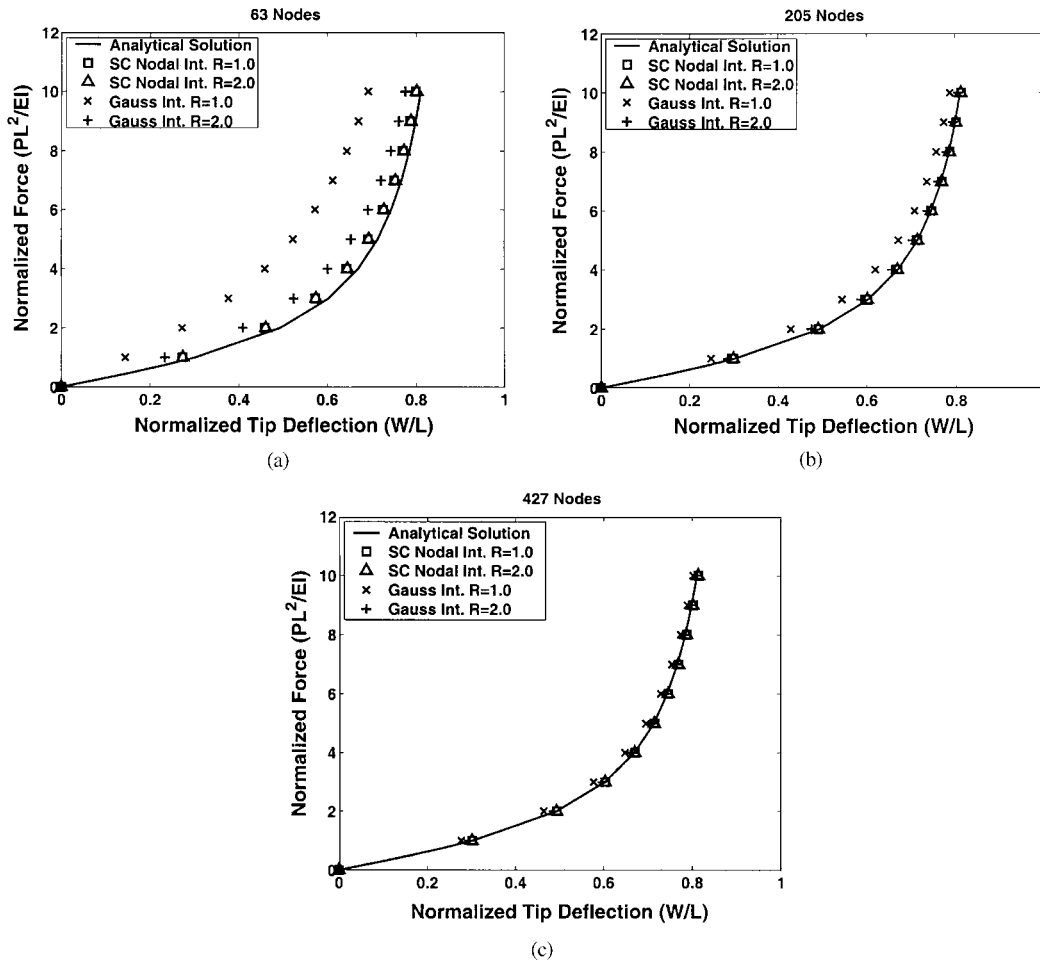


Figure 11. Problem statement of beam problem.

Figure 12. Comparison of SC nodal and Gauss integration methods in beam problem using three discretizations: (a) 21×3 nodes; (b) 41×5 nodes; and (c) 61×7 nodes.

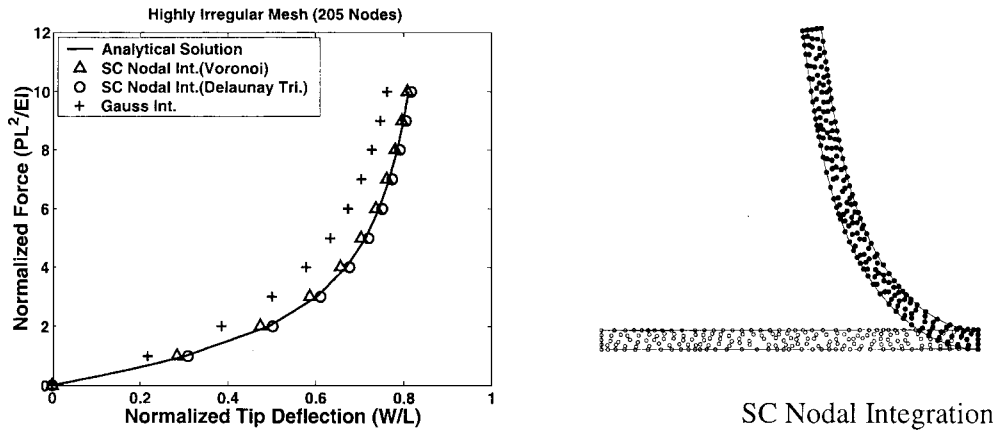


Figure 13. Solution of irregular discretization in beam deflection problem.

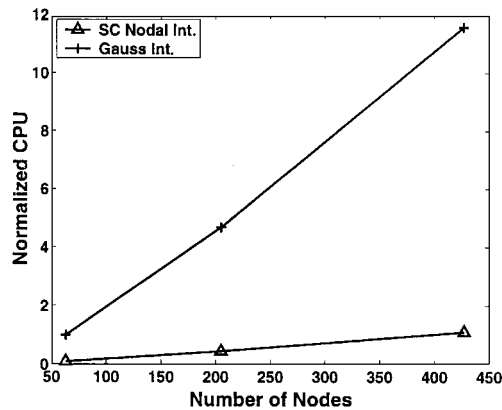


Figure 14. CPU comparison on formation of mesh-free discrete equations.

5.3. Incompressible plane strain tube subjected to an internal pressure

This example examines the performance of SC nodal integration method for nearly incompressible problems. Constraints are introduced in the axial direction to impose the plane-strain condition shown in Figure 15. The tube is made of a Rivlin-type hyperelastic material

$$W = \sum_{m+n=1}^{\infty} A_{mn} (\bar{I}_1 - 3)^m (\bar{I}_2 - 3)^n + \frac{k}{2} (J - 1)^2 \quad \bar{I}_1 = I_1 I_3^{-1/3}, \quad \bar{I}_2 = I_2 I_3^{-2/3}, \quad J = I_3^{1/2} \quad (62)$$

where I_1, I_2, I_3 are the three invariants of Green–Lagrangian strain, and the material constants are $A_{10} = 0.373 \text{ MPa}$, $A_{20} = -0.031 \text{ MPa}$, $A_{30} = 0.005 \text{ MPa}$, and $k = 10^5 \text{ MPa}$ [22]. The high ratio

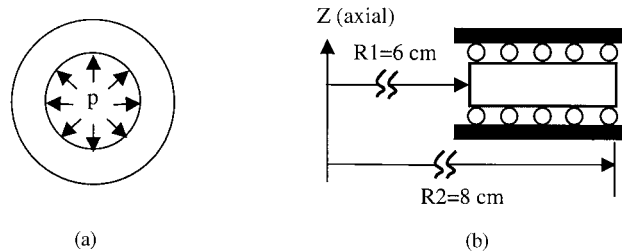


Figure 15. Problem statement of incompressible plane strain tube subjected to internal pressure: (a) original problem; and (b) axisymmetric plane strain model.

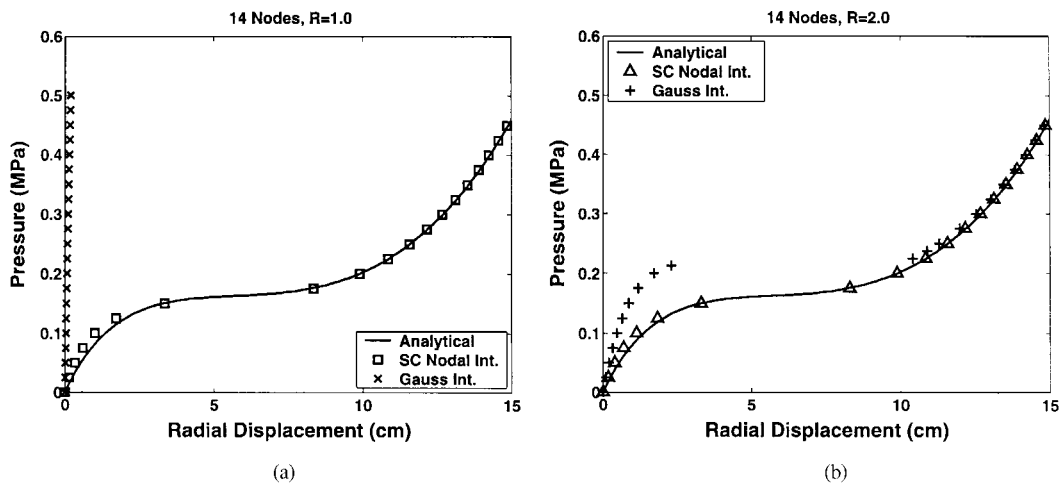


Figure 16. Solutions of the tube inflation problem using a (7×2) -node discretizations with two normalized shape function support sizes: (a) $R = 1.0$; and (b) $R = 2.0$.

of k/A_{mn} introduces incompressibility to the material. The analytical solution of the problem can be found in Stevenson [23].

Owing to the plane strain condition, only two nodes are used in the discretization in the axial z -direction. Two discretization models having 7×2 and 9×2 nodes and two normalized support sizes $R = 1.0$ and 2.0 are used in the analysis. Figures 16 and 17 compare the pressure–displacement curves at the inner wall predicted by the SC nodal integration and 5×5 Gauss integration methods for (7×2) -node and (9×2) -node discretizations, respectively. The results show that a large support size must be used in the Gauss integration method in order to avoid volumetric locking. Similar results have been reported in References [24, 22]. A correction of the over-constrained condition, such as the pressure projection method [22], must be introduced to remove locking in incompressible problems. In contrast, the SC nodal integration provides a locking-free solution despite the use of a small support size for both discretizations as shown

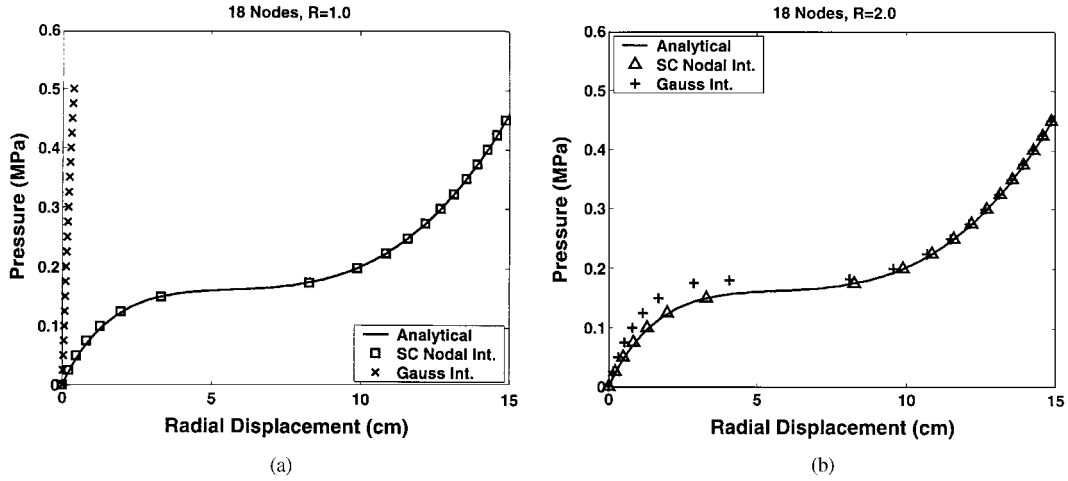


Figure 17. Solutions of the tube inflation problem using a (9×2) -node discretization with two normalized shape function support sizes: (a) $R = 1.0$; and (b) $R = 2.0$.

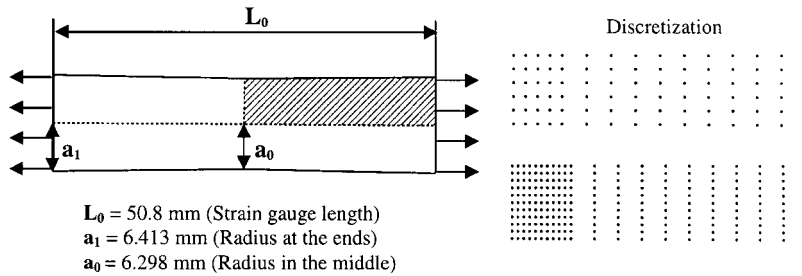


Figure 18. Problem description of a necking problem.

in Figures 16 and 17. When the normalized support size is increased to 3.0, both methods generate highly accurate solutions.

5.4. Necking of a circular bar

This problem is studied to identify the applicability of the proposed method to path-dependent materials. An axisymmetric bar with a length of 53.334 mm and a radius of 6.413 mm is subjected to an axial prescribed displacement. For comparison with experimental data [25], the two ends of the specimen are radially restrained to reflect the actual experimental test fixture. As shown in Figure 18, a geometric imperfection at the center of the rod is introduced to perturb the deformation away from a homogeneous strain state near the centre of the specimen. The rod is assumed to be an elastoplastic material that follows the J_2 flow rule with isotropic hardening as

$$\sigma_y(\bar{\epsilon}^p) = \sigma_y^0 + \alpha \bar{\epsilon}^p + (\sigma_y^\infty - \sigma_y^0)(1 - e^{-\beta \bar{\epsilon}^p}) \quad (63)$$

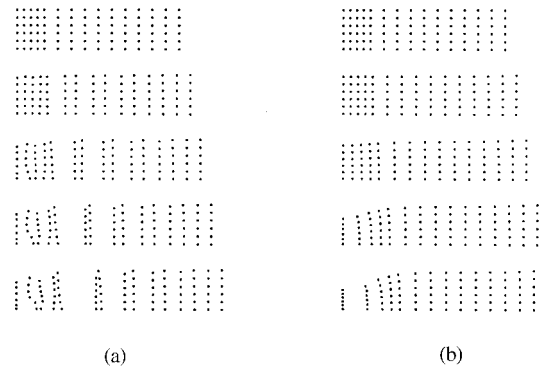


Figure 19. Comparison of progressive deformation (coarse model): (a) direct nodal integration; and (b) stabilized conforming nodal integration.

where σ_y and $\bar{\epsilon}^p$ are yield stress and effective plastic strain, respectively, $\sigma_y^0 = 0.45$ GPa, $\sigma_y^\infty = 0.715$ GPa, $\alpha = 0.12924$ GPa, and $\beta = 16.93$. Other material properties are Young's modulus, $E = 206.9$ GPa, and Poisson's ratio, $\nu = 0.29$ [25].

Multiplicative plasticity with consistent tangent formulation [26] is used in the analysis. Owing to symmetry, only a quarter of the specimen is discretized using both coarse and fine models, as shown in Figure 18. A normalized shape function support size of $R = a/h = 2.0$ (h is the nodal distance) with a smooth transition on the support size a near the interface of the coarse and fine discretization areas is used in the analysis. The analysis proceeds until the total axial displacement reaches 14 mm. The stiffness matrix and force vector are integrated using a direct nodal integration and the stabilized conforming (SC) nodal integration for comparison. The progressive deformation obtained using the coarse model is illustrated in Figure 19. The displacement solution of the direct nodal integration exhibits spatial oscillation in both the axial and transverse directions. A refined discretization near the centroid of the specimen generates a non-physical deformation pattern when a direct nodal integration is used, as shown in Figure 20, where necking occurs near the interface of regions that exhibit substantial difference in nodal density. Spatial instability and non-physical necking are suppressed and corrected using the SC nodal integration as shown in Figures 19 and 20. Good agreement between experimental data and the SC nodal integration solution is shown in Figures 21(a) and 21(b).

5.5. Cylindrical punch of a sheet metal

A plane-strain sheet metal is stretched by a cylindrical punch as shown in Figure 22. The constitutive law of sheet metal is described using a J_2 plasticity with material constants: Young's modulus $E = 69$ GPa, Poisson's ratio $\nu = 0.3$, isotropic hardening $\sigma_y(\bar{\epsilon}^p) = 589(10^{-4} + \bar{\epsilon}^p)^{0.216}$ MPa, and coefficient of friction $\mu = 0$. In this analysis, the end of the sheet metal is fixed, and the rigid punch is moved downward with a vertical displacement of 30 mm in 50 incremental steps. Reproducing kernel contact formulation and kinematic constraint treatments [27] are employed for the contact analysis.

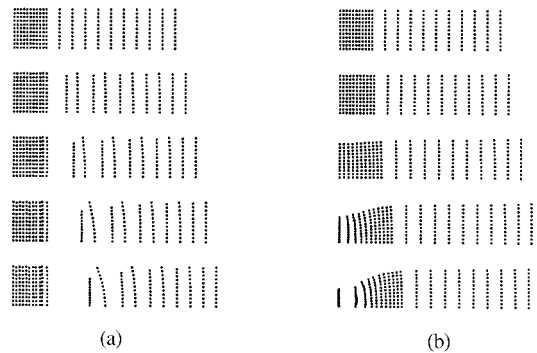


Figure 20. Comparison of progressive deformation (fine model): (a) direct nodal integration; and (b) stabilized conforming nodal integration.

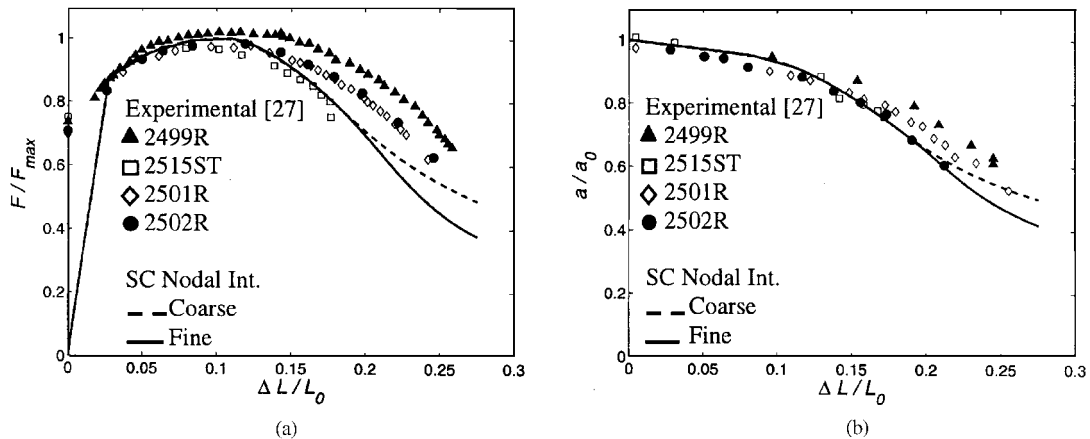


Figure 21. Comparison of mesh-free solution with SC nodal integration with experimental data: (a) load-displacement response; and (b) necking-displacement response.

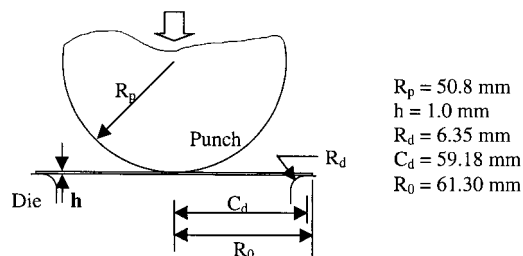


Figure 22. Problem description and half-discretization of a cylindrical punch.

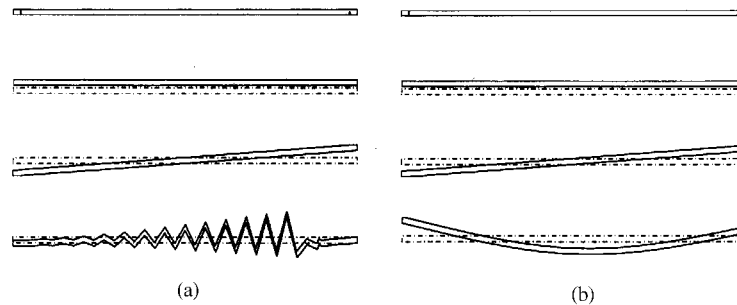


Figure 23. The first four modes of stiffness constructed using direct and SC nodal integrations: (a) direct nodal integration; and (b) stabilized conforming nodal integration.

Owing to symmetry, only half of the sheet metal is modelled as shown in Figure 22. Relatively dense particles are distributed around the die corners in order to capture local necking in those areas. An eigenvalue analysis is first performed. Four zero eigenvalues exist when stiffness matrix is formed using a direct nodal integration. As shown in Figure 23(a), three zero eigenvalues are associated with rigid-body translation and rotation, whereas the fourth zero eigenvalue corresponds to a spurious zero-energy mode. On the other hand, stiffness matrix integrated using SC nodal integration contains only three zero eigenvalues associated with rigid-body motion, and the fourth smallest eigenvalue corresponds to a bending mode as shown in Figure 23(b).

The progressive deformation obtained by the use of a direct nodal integration with a small normalized shape function support size of $R = 1.2$ is illustrated in Figure 24. The severe oscillation in the sheet metal clearly demonstrates the instability in the solution of the direct nodal integration. Non-physical necking also occurs. The proposed SC nodal integration effectively removes the spatial oscillation as shown in Figure 25.

In Figure 26, analyses using a direct nodal integration with increased shape function support sizes $R = 1.2, 2.0, 3.0$ are performed. It is shown in Figure 26 that although the transverse oscillation in the direct nodal integration can be reduced by simply increasing the normalized shape function support size R , this approach does not remove the displacement oscillation in the membrane direction. The SC nodal integration, on the other hand, is capable of generating a stable solution in all cases. The predicted load–displacement responses of the three refinements are compared to the membrane solution [28] in Figure 27. The results show that the SC nodal integration solution agrees well with the membrane solution. Note that the membrane solution does not take necking deformation into consideration. In contrast, a direct nodal integration produces a large error even for a small strain range.

6. CONCLUSION

A formulation has been presented for a stabilization of nodal integration under the Galerkin mesh-free framework for application to problems involving material and geometrical non-linearities. In conjunction with the Lagrangian reproducing kernel (or moving least-squares)

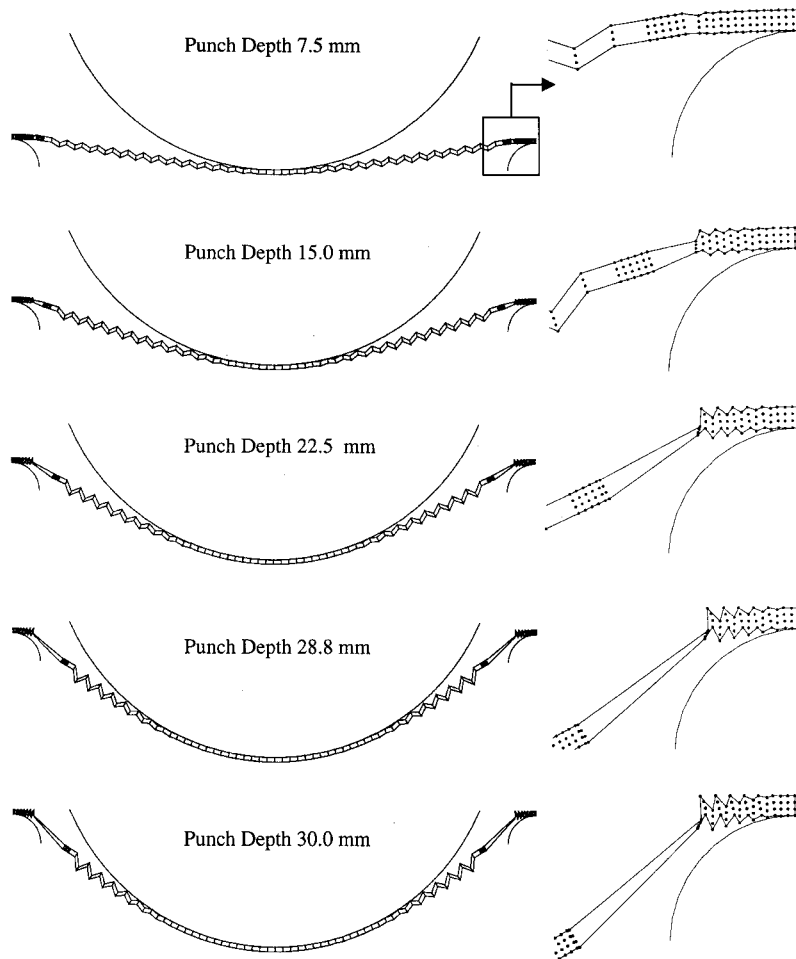


Figure 24. Progressive deformation obtained using a direct nodal integration.

approximations, a Lagrangian strain smoothing is introduced to the deformation gradient as a stabilization for nodal integration of stiffness and internal force in the Galerkin mesh-free method. Employment of a smoothed gradient matrix satisfies the Lagrangian integration constraints associated with the nodal integration of the variational equation formulated in the undeformed configuration.

The proposed strain smoothing stabilization for non-linear problems uses a spatial averaging of the deformation gradient that avoids taking material derivatives of the Lagrangian shape functions directly at the nodes, and hence removes instability in the solution of nodally integrated discrete equations. The proposed method is directly applicable to a total Lagrangian formulation, where the deformation gradient is the primary kinematic variable. For updated Lagrangian formulation, the spatial derivative of displacement is transformed to the material derivative through the inverse of the deformation gradient. Hence, for plasticity, the inverse of

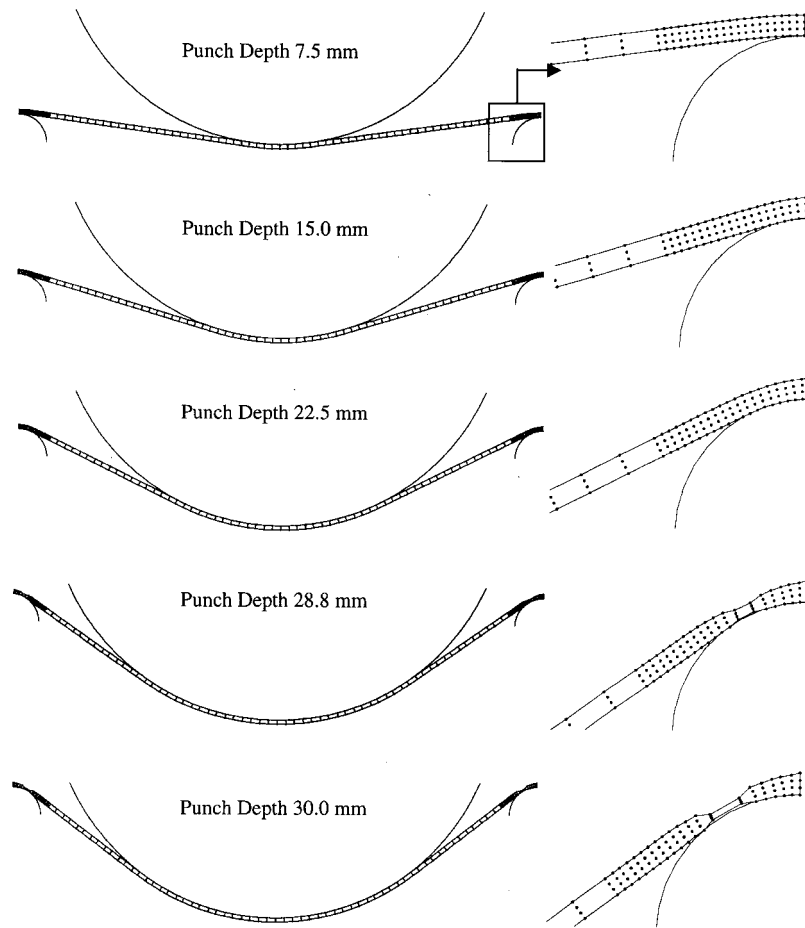


Figure 25. Progress deformation obtained using a stabilize conforming nodal integration.

the deformation gradient also needs to be computed using the smoothed deformation gradient in the stabilization processes.

As discussed in Reference [10], Gauss integration does not satisfy linear exactness in the Galerkin method, even with the employment of a linearly complete reproducing kernel approximation. For this reason, the proposed SC nodal integration provides better accuracy than that of the Gauss integration method. Numerical examples have demonstrated that the SC nodal integration provides significant improvements in accuracy over the Gauss integration method, in particular when a coarse discretization with a small shape function support size is used in the mesh-free analysis. It has also been shown that a severe oscillation in displacement occurs when a direct nodal integration is employed in the construction of stiffness and internal force without stabilization. The presence of plastic deformation magnifies the numerical instability in plasticity. The proposed strain smoothing stabilization effectively suppresses instability in the solution of the direct nodal integration method. By

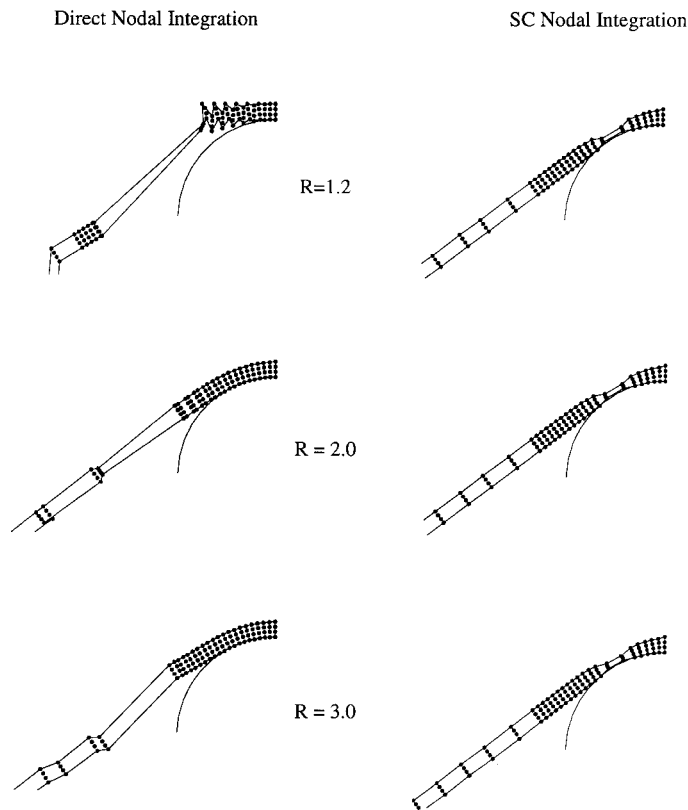


Figure 26. Effect of shape function support size on the numerical instability.

using nodal integration with strain smoothing stabilization, the proposed method is shown to be quite effective for incompressible problems. No incompressible locking is observed even when employing small shape function support sizes. The method also appears to be quite robust in dealing with irregular discretization of the problem domain; the solution accuracy does not seem to exhibit noticeable deterioration when an irregular node distribution is used.

Using SC nodal integration, the formation of the discrete equations is accelerated by an order of magnitude in comparison with the Gauss integration method. Compared to linear problems, higher computational efficiency is gained in non-linear problems, since the strain smoothing stabilization is only performed at the initial stage of non-linear analysis using the Lagrangian mesh-free discretization. In non-linear computation, many state variables must be stored at the integration points. The use of SC nodal integration provides a substantial memory savings, particularly for plasticity. As demonstrated in the numerical examples, high accuracy can be achieved in SC nodal integration even by using a small support size in the shape functions. This property enables solution of a mesh-free discrete equation of higher sparsity, yielding an additional degree of efficiency.

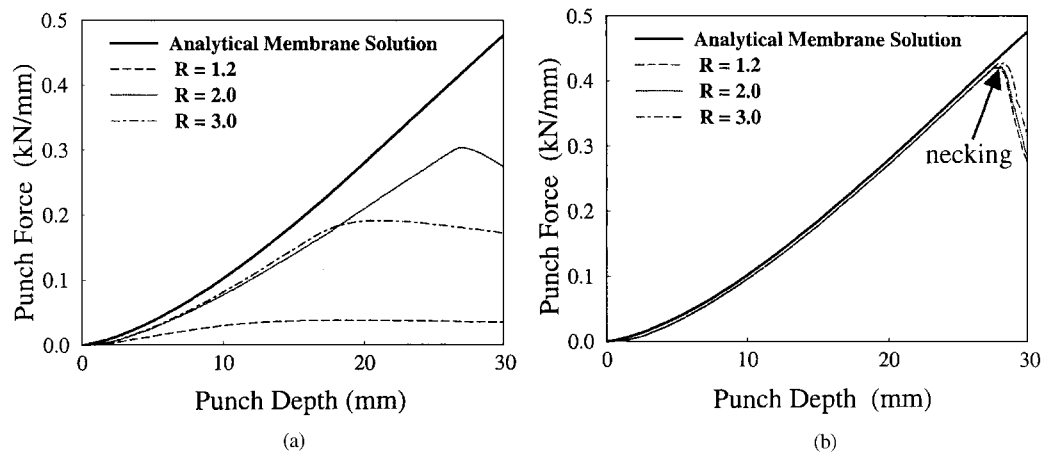


Figure 27. Comparison of the cylindrical punch load–displacement response: (a) direct nodal integration; and (b) stabilized conforming nodal integration.

ACKNOWLEDGEMENTS

The support of this work by NSF under the grant CMS 97-13842 and by the NSF/DARPA OPAAL Program under the grant DMS 98-74015 to the University of Iowa is greatly acknowledged.

REFERENCES

1. Nayroles B, Touzot G, Villon P. Generalizing the finite element method: diffuse approximation and diffuse elements. *Computational Mechanics* 1992; **10**:307–318.
2. Belytschko T, Lu YY, Gu L. Element-free Galerkin methods. *International Journal for Numerical Methods in Engineering* 1994; **37**:229–256.
3. Liu WK, Jun S, Zhang YF. Reproducing kernel particle methods. *International Journal for Numerical Methods in Fluids* 1995; **20**:1081–1106.
4. Belytschko T, Krongauz Y, Fleming M, Organ D, Liu WK. Smoothing and accelerated computations in the element-free Galerkin method. *Journal of Computational and Applied Mathematics* 1996; **74**:111–126.
5. Li S, Liu WK. Reproducing kernel hierarchical partition of unity, Part I: formulation and theory, Part II: applications. *International Journal for Numerical Methods in Engineering* 1999; **45**:251–288, 1999; **45**:289–317.
6. Chen JS, Pan C, Wu CT, Liu WK. Reproducing kernel particle methods for large deformation analysis of non-linear structures. *Computer Methods in Applied Mechanics and Engineering* 1996; **139**:195–227.
7. Duarte CAM, Oden JT. A h-p adaptive method using clouds. *Computer Methods in Applied Mechanics and Engineering* 1996; **139**:237–262.
8. Melenk JM, Babuska I. The partition of unity finite element method: Basic theory and applications. *Computer Methods in Applied Mechanics and Engineering* 1996; **139**:289–314.
9. Dolbow J, Belytschko T. Numerical integration of Galerkin weak form in meshfree methods. *Computational Mechanics* 1999; **23**:219–230.
10. Chen JS, Wu CT, Yoon S, You Y. A stabilized conforming nodal integration for Galerkin meshfree methods. *International Journal for Numerical Methods in Engineering* 2001; **50**:435–466.
11. Krongauz Y, Belytschko T. Consistent Pseudo-derivatives in meshless methods. *Computer Methods in Applied Mechanics and Engineering* 1997; **146**:371–386.
12. Bonet J, Kulasegaram S. Correction and stabilization of smooth particle hydrodynamics methods with applications in metal forming simulation. *International Journal for Numerical Methods in Engineering* 1999; **47**:1189–1214.
13. Randles PW, Libersky LD. Smoothed particle hydrodynamics: some recent improvements and applications. *Computer Methods in Applied Mechanics and Engineering* 1996; **139**:375–408.

14. Johnson GR, Beissel SR. Normalized smoothing functions for impact computations. *International Journal for Numerical Methods in Engineering* 1996; **39**:2725–2741.
15. Beissel S, Belytschko T. Nodal integration of the element-free Galerkin method. *Computer Methods in Applied Mechanics and Engineering* 1996; **139**:49–74.
16. Randles PW, Libersky LD, Petschek AG. On neighbors, derivatives, and viscosity in particle codes. *Proceeding of ECCM Conference*, Munich, Germany, August 31–September 3, 1999.
17. Breitkopf P, Touzot G, Villon P. Double grid diffuse collocation method. *Computational Mechanics* 2000; **25**:199–206.
18. Liszka T, Orkisz J. The finite difference method at arbitrary irregular grids and its application in applied Mechanics. *Computers and Structures* 1980; **11**:83–95.
19. Chen JS, Pan C, Roque C, Wang HP. A Lagrangian reproducing kernel particle method for metal forming analysis. *Computational Mechanics* 1998; **22**:289–307.
20. Schreyer HL, Masur EF. Buckling of shallow arches. *ASCE Journal of Engineering Mechanics Division* 1966; **EM4**:1–19.
21. Timoshenko SP, Gere JM. *Mechanics of Materials*. Van Nostrand Reinhold: New York, 1972.
22. Chen JS, Yoon S, Liu WK. An improved reproducing kernel particle method for nearly incompressible hyperelastic solids. *Computer Methods in Applied Mechanics and Engineering* 2000; **181**:117–146.
23. Stevenson AC. Some boundary value problems of two-dimensional elasticity. *Philosophical Magazine* 1949; **34**:766–793.
24. Chen JS, Wang HP. Some recent improvements in meshfree methods for incompressible finite elasticity boundary value problems with contact. *Computational Mechanics* 2000; **25**:137–156.
25. Norris DM, Moran Jr. B, Scudder JK, Quinones DF. A computer simulation of the tensile test. *Journal of Mechanics and Physics of Solids* 1978; **16**:1–19.
26. Simo JC. A framework for finite strain elastoplasticity based on maximum plastic dissipation and multiplicative decomposition: Part I. Continuum formulation: Part II. computational aspects. *Computer Methods in Applied Mechanics and Engineering* 1988; **66**:199–219, **68**:1–31.
27. Chen JS, Wang HP. New boundary condition treatments for meshless computation of contact problems. *Computer Methods in Applied Mechanics and Engineering* 2000; **187**:441–468.
28. Choudhry S, Lee JK. Dynamic plane-strain element simulation of industrial sheet-metal forming processes. *International Journal of Mechanical Sciences* 1994; **36**:189–207.